Displacement Uncertainty Quantifications in T3-Stereocorrelation

M Berny, T. Archer, P. Beauchêne, A. Mavel, François Hild

Experimental Mechanics manuscript No.
(will be inserted by the editor)

Displacement Uncertainty Quantifications in T3-Stereocorrelation

M. Berny · T. Archer · P. Beauchêne · A. Mavel · F. Hild

Received: date / Accepted: date

Abstract Background: Uncertainty quantifications are required for any measurement result to be meaningful. Objective: The present work aims at deriving and comparing a priori estimates of displacement uncertainties in T3-stereocorrelation for a setup to perform high temperature tests. Methods: Images acquired prior to the actual experiment (*i.e.,* at room temperature) were registered using 3-noded triangular elements (T3-stereocorrelation) to determine displacement uncertainties for different positions of the experimental setup. Results: The displacement uncertainties were then compared to their a priori estimates. Conclusions:

M. Berny and F. Hild*

Université Paris-Saclay, ENS Paris-Saclay, CNRS

LMT - Laboratoire de Mécanique et Technologie, Gif-sur-Yvette, France

*Corresponding author. Email: francois.hild@ens-paris-saclay.fr

T. Archer, P. Beauchêne, A. Mavel

ONERA, Châtillon, France

T. Archer, M. Berny

SAFRAN Ceramics, a technology platform of Safran Tech, Mérignac, France

For the analyzed experiment, it is shown that noise floor estimates only differed by a factor 2 when compared to a posteriori measurements of standard displacement uncertainties.

Keywords Covariance matrix · Displacement · Noise floor level · Uncertainty quantification

1 Introduction

Stereocorrelation is a mature measurement technique [1,2,3]. Most commercial codes use local (*i.e.,* subset-based) analyses to perform spatial and temporal registrations that enable 3D shapes and their deformations to be measured. With such approaches, the output information corresponds to clouds of 3D points (*i.e.,* centers of interrogation windows) and their motions [4,5,6,7]. If comparisons with virtual models are sought, additional steps are required to change the experimental frame to that of the modeler (for CAD models) or the finite element model. To link these two spaces, Iterative Closest Point (ICP) algorithms [8, 9] are one possible route, which may induce additional errors [10].

Another route is to start with the virtual model of the surface of interest, and use the calibration step to globally express the extrinsic and intrinsic parameters of each considered camera in the virtual reference frame [11,12]. There is therefore no additional step required for comparing measured and nominal shapes [12,13,14]. This type of global approach has been applied to NURBS-based [15,16] or finite element [17,13,18] descriptions of the measured shape and its subsequent deformation.

Any stereocorrelation technique calls for uncertainty quantifications if they are used in academia or industry [19,20]. The uncertainties associated with calibration parameters and shape measurements were assessed by propagating acquisition noise [21] and validated in actual configurations [22]. Monte-Carlo simulations were performed to assess in a systematic way the sensitivities to various calibration parameters [23,24]. Further, the effect of

lighting fluctuations and deformations were added [25] and guidelines were proposed to mitigate as much as possible the level of uncertainties [26,20].

Most of the previous analyses focused on calibration and shape measurements. Very recently, displacement uncertainties were assessed for local and global multiview registrations with finite elements. It was shown that the covariance matrix of the measured degrees of freedom was equal to the inverse of the Hessian matrix of the underlying minimization scheme of the suitably normalized cost function [27]. A simplified expression was derived for the standard displacement uncertainty and was validated against artificial test cases. This framework will be further studied for finite element (FE) based stereocorrelation using 3-noded triangles (*i.e.,* T3-stereocorrelation). All these derivations correspond to the so-called Rao and Cramér *lower* bounds [28,29] applied to evaluation of displacement uncertainties.

The paper is organized as follows. The first part deals with a priori estimations of displacement uncertainties in the case of finite element based stereocorrelation when 3-noded elements are utilized. Closed-form expressions are derived by using mean field approximations. In the second part, the so-called BLAG setup [30] is introduced. It allows thermomechanical tests to be performed with a CO_2 laser heating the top surface of plates or beams. The calibration of the stereovision system was performed in a global setting. One of its key features is the fact that the calibration target was kept in the field of view during the whole experiment. Such configuration allows thermal heat wave effects to be quantified in high temperature experiments. In the following analyses, uncertainty quantifications were performed at room temperature prior to such tests. Last, the a priori displacement uncertainties are compared to actual levels measured on the sample surface *and* the calibration target when a series of images for different prescribed displacements were acquired by following the spirit of standard prEN 4861 P1 [19].

2 A Priori Uncertainties in T3-Stereocorrelation

2.1 Covariance in FE-based Stereocorrelation

The following discussion focuses on surfaces of interest discretized with finite elements. The same discretization was assumed for the displacement fields such that a single mesh is needed to describe the surface shape and its deformation. In a multiview framework, the surface of interest is the master information, and each of the $n_c \geq 2$ cameras is calibrated with respect to the reference frame of the numerical model of the n_s surfaces $\mathscr{S}_s$ (or that of the calibration target). Shape corrections were subsequently performed to evaluate offsets between the actual shape and its nominal model. Last, displacement fields were measured by minimizing the following *weighted* cost function

$$\phi_u^2(\{\boldsymbol{U}\}) = \sum_{c=1}^{n_c} \sum_{j=1}^{n_s} \sum_{\boldsymbol{X}_j \in \mathscr{S}_j} \omega_j^c \, \frac{(I_t^c(\boldsymbol{x}^c + \boldsymbol{u}^c(\{\boldsymbol{U}\})) - I_0^c(\boldsymbol{x}^c))^2}{2(\sigma^c)^2} \tag{1}$$

with respect to the unknown degrees of freedom $\{\boldsymbol{U}\}$ for the series of images in the deformed configuration I_t^c with respect to those in the reference configuration I_0^c. The weight ω_j^c is equal to 1 when the surface $\mathscr{S}_j$ is visible by the camera c, and null otherwise. The variance $(\sigma^c)^2$ describes the level of acquisition noise at each evaluation point $\boldsymbol{X}_s$ of the cost function [27]. In the present setting, acquisition noise is assumed to Gaussian and white at the pixel level. If it were Poissonian instead (*i.e.,* variance proportional to the gray level), the Anscombe transform could be used to account for such effect [31,32,33].

The considered surfaces of interest $\mathscr{S}_j$ are projected onto each camera c plane as surfaces $\mathscr{S}_j^c$ thanks to the projection matrices $[\boldsymbol{P}^c]$ that relate the homogeneous coordinates of 3D points $\{\boldsymbol{X}_j\}$ to their pixel positions $\{\boldsymbol{x}^c\}$

$$s^c\{\boldsymbol{x}^c\} = [\boldsymbol{P}^c]\{\boldsymbol{X}_j\} \tag{2}$$

where s^c is the local scale factor. In the present setting, the apparent pixel displacement $\boldsymbol{u}^c$ depends on the nodal displacement vector $\{\boldsymbol{U}\}$. The framework (1) enables an *arbitrary number* of cameras (*i.e.,* $n_c \geq 2$) to be considered, in a similar fashion as standard stereocorrelation (*i.e.,* $n_c = 2$).

The minimization of the cost function ϕ_u^2 (Equation (1)) is performed via a modified Gauss-Newton scheme [34, 1, 35] that consists in iteratively updating the nodal corrections $\{\delta\boldsymbol{U}\}$ through the solution to the global system

$$\left(\sum_{c=1}^{n_c}[\boldsymbol{H}^c]\right)\{\delta\boldsymbol{U}\} = \sum_{c=1}^{n_c}\{\boldsymbol{h}^c\} \tag{3}$$

where $[\boldsymbol{H}^c]$ denotes the Hessian matrix associated with each camera c

$$H_{ij}^c = \sum_{j=1}^{n_s}\sum_{\mathscr{S}_j^c}\omega_j^c\,\frac{(\boldsymbol{\nabla} I_0^c\cdot\boldsymbol{\varphi}_i^c)(\boldsymbol{\nabla} I_0^c\cdot\boldsymbol{\varphi}_j^c)}{2(\sigma^c)^2} \tag{4}$$

in which the dependence on $\boldsymbol{x}^c$ in the summand was omitted for the sake of simplicity, and $\{\boldsymbol{h}^c\}$ the residual vector

$$h_j^c = \sum_{j=1}^{n_s}\sum_{\mathscr{S}_j^c}\omega_j^c\,\frac{\rho^c(\boldsymbol{\nabla} I_0^c\cdot\boldsymbol{\varphi}_j^c)}{2(\sigma^c)^2} \tag{5}$$

with $\boldsymbol{\varphi}_k^c$ the kinematic sensitivity of the k-th degree of freedom U_k along direction $\boldsymbol{e}_k$ (no index summation)

$$\boldsymbol{\varphi}_k^c = [\boldsymbol{\Pi}^c(\boldsymbol{X})]\boldsymbol{e}_k N_k(\boldsymbol{X}) \tag{6}$$

where N_k denotes the shape function of nodal displacement U_k, and $[\boldsymbol{\Pi}^c] = \partial\boldsymbol{x}_c/\partial\boldsymbol{X}$ the *placement sensitivities*. The gray level residual ρ^c is computed for each evaluation point $\boldsymbol{x}^c$ and current estimate of the nodal displacement vector $\{\widetilde{\boldsymbol{U}}\}$

$$\rho^c(\boldsymbol{x}^c) = I_t^c(\boldsymbol{x}^c + \boldsymbol{u}^c(\{\widetilde{\boldsymbol{U}}\})) - I_0^c(\boldsymbol{x}^c) \tag{7}$$

In the following, the uncertainty quantifications accounting for acquisition noise are performed on the displacement fields only. Other sources of errors related to calibration

and shape corrections are not accounted for herein. The covariance matrix of the measured degrees of freedom $[\boldsymbol{C}] = \langle \{\delta \boldsymbol{U}\} \{\delta \boldsymbol{U}\}^\top \rangle_\eta$ (where $\langle \cdot \rangle_\eta$ denotes the expected value over noise η) then reduces to [27]

$$[\boldsymbol{C}] = [\boldsymbol{H}]^{-1} \tag{8}$$

where $[\boldsymbol{H}]$ is the total Hessian of the multiview correlation scheme

$$[\boldsymbol{H}] = \sum_{c=1}^{n_c} [\boldsymbol{H}^c] \tag{9}$$

when the gray level residuals are assumed to be only due to white Gaussian noise (*i.e.,* $\rho^c = \eta^c$) of variance $2(\sigma^c)^2$. If the mean gray level of Gaussian noise is equal to zero, then the displacement estimates are unbiased. When (iterative) Gauss-Newton schemes are considered to perform the minimization of Equation (1), the global Hessian matrix $[\boldsymbol{H}]$ is computed. Consequently, the covariance matrix $[\boldsymbol{C}]$ is directly known since it simply is the inverse of $[\boldsymbol{H}]$ in the present setting.

The next sections aim at deriving closed-form solutions for various meshes using 3-noded triangles (*i.e.,* T3-stereocorrelation). The basis of the derivations consists in mean field approximations of the various terms needed to calculate the Hessian matrices [27]. Long-range (*i.e.,* $[\boldsymbol{\Pi}^c(\boldsymbol{X})]\boldsymbol{e}_k$) and short range (*i.e.,* $\boldsymbol{\nabla} I_0^c$) fluctuations are separated from those of the shape functions N_k. Consequently, the integral of the tensor $\boldsymbol{\nabla} I_0^c \otimes \boldsymbol{\nabla} I_0^c$ is approximated by $S_k^c/2\langle \|\boldsymbol{\nabla} I_0^c\|_2^2 \rangle \boldsymbol{I}$, where $\boldsymbol{I}$ is the identity tensor, and S_k^c the area of the projected support surface of the shape function N_k. Further, Π_k^c denotes the mean placement (pixel/m) sensitivity for the studied component of displacement. With such hypotheses, a first order estimate of the diagonal terms of the Hessian matrix becomes

$$H_{kk} \propto N_{eq}^2 \sum_{c=1}^{n_c} \frac{(\Pi_k^c)^2 \langle \|\boldsymbol{\nabla} I_0^c\|_2^2 \rangle}{4(\sigma^c)^2} \tag{10}$$

and the variance $\sigma_k^2 = C_{kk}$ of the nodal displacement U_k uncertainty is proportional to $1/H_{kk}$, or equivalently

$$\sigma_k^2 \propto \frac{1}{N_{eq}^2} \left(\sum_{c=1}^{n_c} \frac{(\Pi_k^c)^2 \langle \|\boldsymbol{\nabla} I_0^c\|_2^2 \rangle}{4(\sigma^c)^2} \right)^{-1} \tag{11}$$

where Π_k^c denotes the mean placement (pixel/m) sensitivity for the studied component of displacement, and N_{eq} the equivalent number of integration points (*i.e.,* the square root of the total number of integration points per element N_{IP}^2). Equations (10) and (11) show that when more than 2 cameras are used (*i.e.,* multiview systems), and if some regions are imaged by $n_c > 2$ of them, then the measurement uncertainties can be lowered in comparison to a situation with $n_c = 2$ (*i.e.,* stereovision setup). In the following, a more detailed analysis will be performed in the case of meshes made of 3-noded (T3) elements. For the sake of simplicity, it is assumed that the whole studied surface $\mathscr{S}$ is visible by both cameras (*i.e.,* $\omega_j^c = 1$ and $n_c = 2$).

2.2 Local T3-based Stereocorrelation

The previous mean field approximations are utilized to derive the results for a single T3 element (Figure 1(a)). As a consequence, the components $(H_l^c)_{ij}$ of elementary Hessian matrices for each direction $\boldsymbol{e}_k$ are products of shape functions $N_i(x,y)N_j(x,y)$ for $i,j = 1,2,3$ to be integrated over the domain $\mathscr{S}_e^c$ covered by each element

$$[\boldsymbol{H}_l^c] = \frac{N_{eq}^2 (\Pi_k^c)^2 \langle \|\boldsymbol{\nabla} I_0^c\|_2^2 \rangle}{4(\sigma^c)^2} \frac{1}{12} \begin{bmatrix} 2 & 1 & 1 \\ 1 & 2 & 1 \\ 1 & 1 & 2 \end{bmatrix} \tag{12}$$

with $N_1(x,y) = 1-x-y$, $N_2(x,y) = x$, and $N_3(x,y) = y$ following the node numbering and the reference frame of Figure 1(a). In practice, N_{IP} integration points are considered to evaluate the integrals over each element, and N_{eq} denotes the equivalent number of integration points (*i.e.,* the square root of N_{IP}). The total Hessian matrix $[\boldsymbol{H}]$ then becomes a block

diagonal matrix made of $[\boldsymbol{H}_k]$ matrices

$$[\boldsymbol{H}_k] = N_{eq}^2 \sum_{c=1}^{n_c} \frac{(\Pi_k^c)^2 \langle \|\boldsymbol{\nabla} I_0^c\|_2^2 \rangle}{4(\sigma^c)^2} [\boldsymbol{H}_l] \tag{13}$$

where $[\boldsymbol{H}_l]$ is the corresponding dimensionless Hessian matrix (Figure 1(b))

$$[\boldsymbol{H}_l] = \frac{1}{12} \begin{bmatrix} 2 & 1 & 1 \\ 1 & 2 & 1 \\ 1 & 1 & 2 \end{bmatrix} \tag{14}$$

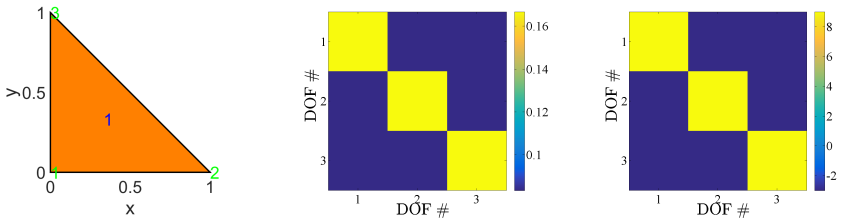

(a) (b) (c)

Fig. 1 (a) T3 element. The node numbering is in green, and that of the element in blue. (b) Dimensionless Hessian matrix $[\boldsymbol{H}_l]$. (c) Corresponding dimensionless covariance matrix $[\boldsymbol{C}_l]$.

The covariance matrix $[\boldsymbol{C}]$ is composed of block diagonal matrices $[\boldsymbol{C}_k]$, which each are the inverse of $[\boldsymbol{H}_k]$

$$[\boldsymbol{C}_k] = \frac{1}{N_{eq}^2} \left(\sum_{c=1}^{n_c} \frac{(\Pi_k^c)^2 \langle \|\boldsymbol{\nabla} I_0^c\|_2^2 \rangle}{4(\sigma^c)^2} \right)^{-1} [\boldsymbol{C}_l] \tag{15}$$

where the dimensionless matrix $[\boldsymbol{C}_l]$ reads (Figure 1(c))

$$[\boldsymbol{C}_l] = 3 \begin{bmatrix} 3 & -1 & -1 \\ -1 & 3 & -1 \\ -1 & -1 & 3 \end{bmatrix} \tag{16}$$

Figure 2(a) shows the diagonal components of the dimensionless covariance matrix $[\boldsymbol{C}_l]$ (*i.e.,* the dimensionless variances of each degree of freedom considered independently of

the others). In the present case, they are identical and equal to 9. This level will serve as comparison when different discretizations are considered.

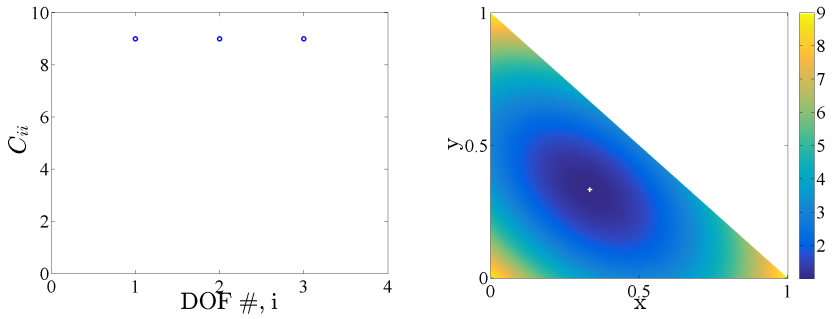

(a) (b)

Fig. 2 (a) Diagonal components (*i.e.,* variances) of the dimensionless covariance matrix $[\boldsymbol{C}_l]$. (b) Dimensionless variance $\sigma_u^2(x,y)$. The white cross shows the location of the minimum level.

Given the fact that the displacement component $U_k^e(x,y)$ of any point (x,y) within the considered T3-element is a linear combination of shape functions N_i and nodal displacements U_i^e

$$U_k^e(x,y) = \sum_{i=1}^{3} N_i(x,y) U_i^e \tag{17}$$

or equivalently, when gathering the shape functions in the column vector $\{\boldsymbol{N}(x,y)\}$

$$U_k^e(x,y) = \{\boldsymbol{N}(x,y)\}^\top \{\boldsymbol{U}^e\} \tag{18}$$

its variance $\sigma^2_{U_k^e}(x,y)$ reads

$$\sigma^2_{U_k^e}(x,y) = \{\boldsymbol{N}(x,y)\}^\top [\boldsymbol{C}_k] \{\boldsymbol{N}(x,y)\} \tag{19}$$

and becomes

$$\sigma^2_{U_k^e}(x,y) = \frac{1}{N_{eq}^2} \left(\sum_{c=1}^{n_c} \frac{(\Pi_k^c)^2 \langle \|\boldsymbol{\nabla} I_0^c\|_2^2 \rangle}{4(\sigma^c)^2} \right)^{-1} \sigma_u^2(x,y) \tag{20}$$

where σ_u^2 denotes the dimensionless variance

$$\sigma_u^2(x,y) = 3\left(4N_1^2(x,y) + 4N_2^2(x,y) + 4N_3^2(x,y) - 1\right) \tag{21}$$

Figure 2(b) shows that the variance σ_u^2 reaches its maximum level (*i.e.,* 9) at each node and its minimum (*i.e.,* 1) at the center of gravity of the T3 element. If only one point were to be kept from local analyses using T3 elements, its center of gravity has the lowest uncertainty in comparison to any other point within the element. Conversely, the nodal displacements have the highest uncertainties.

Last, let us define the spatial resolution. It corresponds to the square root of the surface area used to evaluate any degree of freedom. For one single element, the spatial resolution then is the square root of the area of the domain $\mathscr{S}_e$.

2.3 Global T3-based Stereocorrelation

When using structured meshes made of T3 elements, the connectivity of an inner node is typically equal to 6 (see node 1 of Figure 3(a)). This means that the evaluation of the corresponding nodal displacements is performed over 6 elements. Consequently, the spatial resolution for node 1 is $\sqrt{6}$ times higher than in the case of a single element (Figure 1(a)).

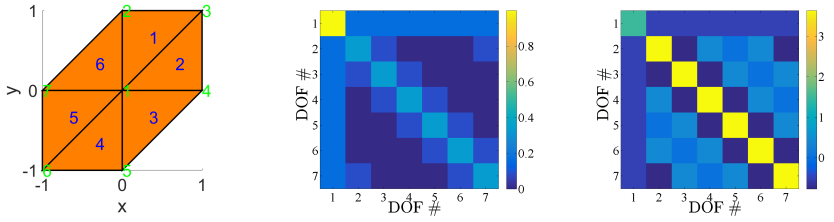

(a) (b) (c)

Fig. 3 (a) Mesh composed of 6 T3 elements. The node numbering is in green, and that of the elements in blue. (b) Dimensionless Hessian matrix $[\boldsymbol{H}_g]$. (c) Corresponding dimensionless covariance matrix $[\boldsymbol{C}_g]$.

The global Hessian matrix $[\boldsymbol{H}]$ of the present mesh is the assembly of all 6 local Hessian matrices for each camera c accounting for node connectivities. As for the local Hessian matrix, it is a block diagonal matrix whose components $[\boldsymbol{H}_k]$ now become

$$[\boldsymbol{H}_k] = N_{eq}^2 \sum_{c=1}^{n_c} \frac{(\Pi_k^c)^2 \langle \|\boldsymbol{\nabla} I_0^c\|_2^2 \rangle}{4(\sigma^c)^2} [\boldsymbol{H}_g] \tag{22}$$

with the dimensionless Hessian matrix $[\boldsymbol{H}_g]$ (Figure 3(b))

$$[\boldsymbol{H}_g] = \frac{1}{12} \begin{bmatrix} 12 & 2 & 2 & 2 & 2 & 2 & 2 \\ 2 & 4 & 1 & 0 & 0 & 0 & 1 \\ 2 & 1 & 4 & 1 & 0 & 0 & 0 \\ 2 & 0 & 1 & 4 & 1 & 0 & 0 \\ 2 & 0 & 0 & 1 & 4 & 1 & 0 \\ 2 & 0 & 0 & 0 & 1 & 4 & 1 \\ 2 & 1 & 0 & 0 & 0 & 1 & 4 \end{bmatrix} \tag{23}$$

From the assembled Hessian matrix, the covariance matrix $[\boldsymbol{C}]$, which is obtained by following the same path as in the previous section, is composed of block diagonal matrices $[\boldsymbol{C}_k]$

$$[\boldsymbol{C}_k] = \frac{1}{N_{eq}^2} \sum_{c=1}^{n_c} \left(\frac{(\Pi_k^c)^2 \langle \|\boldsymbol{\nabla} I_0^c\|_2^2 \rangle}{4(\sigma^c)^2} \right)^{-1} [\boldsymbol{C}_g] \tag{24}$$

where the dimensionless matrix $[\boldsymbol{C}_g]$ reads (Figure 3(c))

$$[\boldsymbol{C}_g] = \frac{1}{30} \begin{bmatrix} 45 & -15 & -15 & -15 & -15 & -15 & -15 \\ -15 & 109 & -23 & 13 & 1 & 13 & -23 \\ -15 & -23 & 109 & -23 & 13 & 1 & 13 \\ -15 & 13 & -23 & 109 & -23 & 13 & 1 \\ -15 & 1 & 13 & -23 & 109 & -23 & 13 \\ -15 & 13 & 1 & 13 & -23 & 109 & -23 \\ -15 & -23 & 13 & 1 & 13 & -23 & 109 \end{bmatrix} \tag{25}$$

Figure 4(a) shows the diagonal components of the dimensionless covariance matrix $[\boldsymbol{C}_g]$. For the central node, the variance is equal to $3/2$, which is six times lower than the levels observed when only one element was considered (Figure 4(a)). This factor 6 decrease is related to the connectivity of this node (*i.e.,* 6) and the increase by a factor $\sqrt{6}$ of the spatial resolution. Conversely, the other nodes have variances that are identical and equal to $109/30 \approx 3.63$.

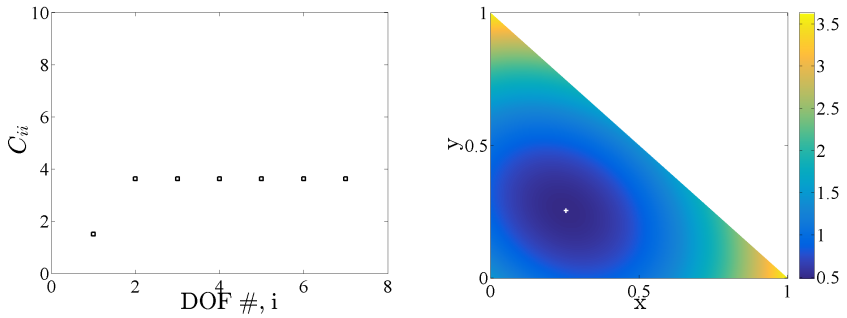

(a) (b)

Fig. 4 (a) Diagonal components of the dimensionless covariance matrix $[\boldsymbol{C}_g]$. (b) Dimensionless variance $\sigma_u^2(x,y)$ for element 1 (Figure 3(a)). The white cross shows the location of the minimum level.

The dimensionless variance σ_u^2 is computed by using Equation (19) in which the block diagonal matrix $[\boldsymbol{C}_k]$ is restricted to the nodes belonging to any of the considered elements. In the present case, the results are identical for all the elements

$$\begin{aligned}\sigma_u^2(x,y) = \frac{1}{30}\big(&45N_1^2(x,y) + 109N_\alpha^2(x,y) \\ &+ 109N_\beta^2(x,y) - 30N_1(x,y)N_\alpha(x,y) \\ &-46N_1(x,y)N_\beta(x,y) - 46N_\alpha(x,y)N_\beta(x,y)\big)\end{aligned} \tag{26}$$

where α,β denote the other two node numbers of any element containing node 1 (*e.g.,* $\alpha=2,\beta=3$ for the element shown in Figure 4(b)). Figure 4(b) shows that the variance σ_u^2

reaches its maximum level (*i.e.,* $109/30 \approx 3.63$) at each edge node and its minimum (*i.e.,* $29/60 \approx 0.48$) at a point that is no longer the center of gravity of the element (in the shown example, it is when $x = y = 0.25$). The nodal displacements have higher uncertainties but their level depends upon the connectivity number.

This first analysis shows the benefit of considering a mesh instead of independent elements, namely, the nodal uncertainties are significantly reduced in comparison with local analyses using independent elements. In the present case, the variance is reduced by a factor 6, which is related to the number of connectivities of the studied (inner) node. The other (edge) nodes also experience uncertainty reductions, yet to a lesser degree (*i.e.,* a factor 2.5) because they share less elements. The minimum variance is also lowered but less (*i.e.,* by a factor of 2.1) than that of nodes.

To further discuss the role of inner, edge and corner nodes, let us consider a simple mesh made of 18 elements (Figure 5(a)). The corresponding dimensionless Hessian matrix $[\boldsymbol{H}_{16}]$ is shown in Figure 5(b). Its maximum value is still equal to 1 (for the inner nodes 6, 7, 10 and 11). However, the minimum value is equal to $1/6$ for nodes 4 and 13, and $1/3$ for nodes 1 and 16. Even though these four nodes are corners, the first ones only belong to one element as opposed to the latter ones. Consequently, the spatial resolution is $\sqrt{2}$ times lower for the former ones. All edge nodes (*i.e.,* 2, 3, 5, 8, 9, 12, 14, 15) have the same (*i.e.,* $1/2$) level as they are all being shared by three elements.

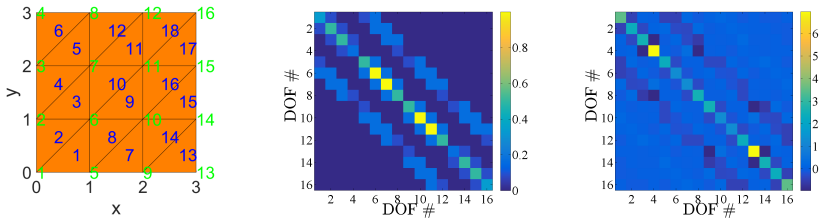

(a) (b) (c)

Fig. 5 (a) Mesh composed of 18 T3 elements. The node numbering is in green, and that of the elements in blue. (b) Dimensionless Hessian matrix $[\boldsymbol{H}_{16}]$. (c) Corresponding dimensionless covariance matrix $[\boldsymbol{C}_{16}]$.

The previous observations also apply to the covariance matrix, whose dimensionless block diagonal component $[\boldsymbol{C}_{16}]$ is shown in Figure 5(c). The inner nodes have about the same level (*i.e.,* ≈ 1.27), the edge nodes $\approx 2.36-2.53$, and the corner nodes either ≈ 3.48 or ≈ 6.96.

When the number of elements is increased, asymptotic results can be obtained. Figure 6(b) shows the diagonal terms of the dimensionless covariance matrix when 2×10^4 elements are considered in a structured mesh (Figure 6(a)). For inner nodes, the dimensionless variance tends to ≈ 1.16. For edge nodes with three connectivities, the asymptotic level is ≈ 2.32. For corner nodes, the dimensionless variance tends to ≈ 6.96 when only one connectivity is concerned, and ≈ 3.48 when it is shared by two elements.

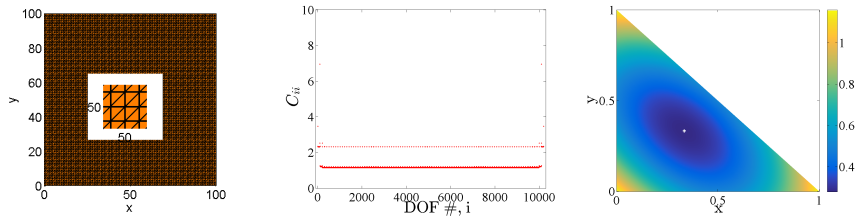

(a) (b) (c)

Fig. 6 (a) Mesh composed of 2×10^4 T3 elements. The inset shows the mesh fineness. (b) Diagonal components of the dimensionless covariance matrix. (c) Dimensionless variance $\sigma_u^2(x,y)$ for one inner element. The white cross shows the location of the minimum level.

2.4 First Order Estimates

All the previous results are now summarized. It is worth remembering that in order to fully quantify the uncertainties, the covariance matrix should be used and reported [19]. When dealing with T3 elements, even in local analyses, it was shown that covariances arose (*i.e.,* off-diagonal terms in the covariance matrices, see Equation (16)). Consequently, the total Hessian matrix accounts for acquisition noise when white and Gaussian.

When simplified assessments are aimed for, the mean variance of each displacement component is a good first order estimate. Further, when using mean field approximations, Equation (11) provides a very simple way of assessing the variance of the degree of freedom U_k. For inner nodes of a structured T3 mesh, it was shown above that the uncertainty level corresponds to a *lower bound* since the connectivity number is the highest (*i.e.,* the corresponding spatial resolution is also the highest). For corner and edge nodes, their spatial resolution is lower than that of inner nodes. Thus, their variances increase. For instance, a multiplicative factor $\sqrt{2}$ is expected for edge nodes sharing three elements. For corner nodes with a connectivity of 2, this factor is equal to $\sqrt{3}$, and for those belonging to one element, $\sqrt{6}$.

Last, let us note that the lowest dimensionless variance level in T3 elements could be decreased from 1 for a single element to 0.28 for a fine mesh. The gain is not as important as for the nodal displacements. Such trend was already observed in Q4-DIC [36]. It can be understood by the fact that the (anti)covariances are lower (in absolute value) compared to the variances in the case of fine meshes than for a single element.

3 Experimental Configuration

3.1 BLAG Setup

The BLAG setup (*Banc Laser A Gradients,* i.e., *laser bench with temperature gradients)* at ONERA [30] was used to analyze the thermomechanical behavior of SiC/SiC composites. A parallelepipedic sample made of CERASEP® A600 Ceramic Matrix Composite (CMC) was manufactured by SAFRAN Ceramics [37]. It was heated at very high temperatures thanks to a CO_2 laser beam [38]. Under such thermal gradients, the material expands and deflects. To measure the thermomechanical fields of the sample, a set of three cameras was installed (Figure 7).

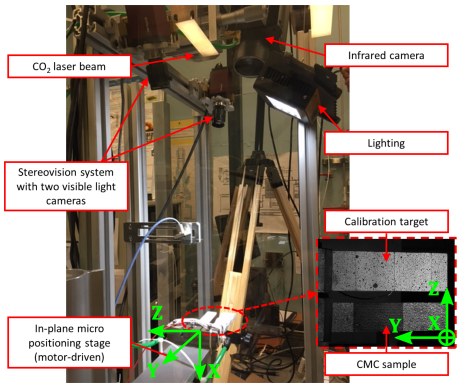

Fig. 7 Multi-instrumented experiment of a SiC/SiC composite under thermal gradient obtained with a CO_2 laser beam. The reference frame (X,Y,Z), where the 3D displacements will be expressed, is depicted with green arrows.

These three cameras monitored the top surface of the studied CMC, which was heated by the laser beam, in order to measure temperature fields during the test (with an infrared camera FLIR X6580sc®, acquiring frames at a frequency of 1 Hz) and 3D surface displacement fields (*i.e.,* stereovision system composed of two cameras, see Table 1). An LED light panel (7700 lm) was installed. Table 1 summarizes the hardware parameters of the stereovision system to be studied herein.

Table 1 DIC hardware parameters of the stereosystem

Cameras	AVT Pike-421
Definition	2048×2048 pixels (B/W images)
Color filter	none
Gray Levels rendering	8 bits
Lens	Schneider Kreuznach 2.8/50 mm
Aperture	f/11
Field of view	16,800 mm^2
Image scale	≈ 63 µm/pixel
Stereo-angle	30°
Stand-off distance	80 cm
Image acquisition rate	0.5 fps
Patterning technique	W or B/W paints (see text)
Pattern feature size	4 px

To measure the 3D surface displacements of the heated face, the CMC sample surface was speckled with a white paint that is resistant to very high temperatures [39]. It is worth noting that the top surface was only partially speckled, with a raw central part corresponding to the heated area and speckled parts on both sides (Figure 25). Therefore, the speckle pattern did not perturb temperature field measurements in the hottest area and the displacements

were measured on both sides of that part (especially on the free edge, where the amplitude of displacements is the highest). In addition, a tailored calibration target (Appendix A) was kept next to the sample, so that it was totally seen by both cameras during the whole experiment. It was also speckled by B/W paints (Figure 17).

The characteristic speckle size, which was determined as the full width at half maximum of the autocorrelation of the regions of interest (ROI) of the calibration target and the speckled part of the sample surface, was equal to 4 px (or ≈ 250 µm). Another quantity is needed, namely, the RMS image gradient $\sqrt{\langle \|\boldsymbol{\nabla} I_0^c\|_2^2 \rangle}$, which was determined over the two ROIs and for both cameras. For the calibration target, it was found equal to 19.4 gray level/px for both cameras. This level was even higher for the CMC sample surface: 22.6 gray level/px for the first camera, and 23.6 gray level/px for the second one.

Last, a fan (not shown in Figure 7) that can be turned on and off was positioned in front of the sample free edge. A reference frame (X,Y,Z) (depicted with green arrows in Figure 7) was defined for that experiment, so that the in-plane motions of the sample correspond to the Y and Z components measured by stereocorrelation, and the out-of-plane displacements to the X component.

3.2 Calibration

In the present case, two calibration steps were needed. First, the cameras were calibrated using the calibration target. Within the present framework, this step (see Appendix B) consisted in determining the projection matrices $[\boldsymbol{P}^c]$ that allow the cameras to be positioned within the updated model of the calibration target (Appendix A) by only using the first pair of acquired images. All other image pairs were used for uncertainty quantification (UQ) purposes.

The second step (Appendix C) was devoted to the positioning of the CMC sample surface in the reference frame of the calibration target. At the end of these two steps, a unique reference frame defines the experimental configuration (*i.e.,* both meshes were positioned with respect to each other), and all the subsequent measurements are expressed in that frame.

3.3 Placement sensitivity fields

Once the projection matrices $[\boldsymbol{P}^c]$ are known (*i.e.,* the stereosystem is calibrated), the placement sensitivity matrices $[\Pi^c(\boldsymbol{X})]$ can be evaluated at any location of the surface of interest. Figure 8 illustrates the placement sensitivity fields (*i.e.,* norms of $\partial \boldsymbol{x}^c/\partial X$, $\partial \boldsymbol{x}^c/\partial Y$, and $\partial \boldsymbol{x}^c/\partial Z$) for the two cameras, and the global (*i.e.,* RMS) sensitivities drawn on the meshes of the nominal surfaces of the CMC sample and calibration target.

These fields, as assumed in the mean field approximation, do not vary much over the region of interest of the CMC sample (more over the calibration target due to its roof top shape), and are, on average, more than 3 times higher in the in-plane directions in comparison with those in the out-of-plane directions. This information is very useful, for instance, when designing experiments and having to place cameras in an optimal way (*i.e.,* minimizing the measurement uncertainties [40]).

On a more quantitative basis, the total out-of-plane RMS sensitivity $\sqrt{\langle \|\partial \boldsymbol{x}/\partial X\|^2 \rangle} =$ 7.2 mpx/µm is about 3.1 times lower than the in-plane components $\sqrt{\langle \|\partial \boldsymbol{x}/\partial Y\|^2 \rangle} =$ 22.3 mpx/µm and $\sqrt{\langle \|\partial \boldsymbol{x}/\partial Z\|^2 \rangle} = 22.6$ mpx/µm for the calibration target. For the CMC surface, the in-plane sensitivities are very close, namely, $\sqrt{\langle \|\partial \boldsymbol{x}/\partial Y\|^2 \rangle} =$ 22.1 mpx/µm and $\sqrt{\langle \|\partial \boldsymbol{x}/\partial Z\|^2 \rangle} = 22.5$ mpx/µm. Conversely, the out-of-plane component $\sqrt{\langle \|\partial \boldsymbol{x}/\partial X\|^2 \rangle} = 6.7$ mpx/µm is lower (*i.e.,* the out-of-plane sensitivity is about 3.3 times lower than the in-plane component). This is due to the fact that the sample surface is

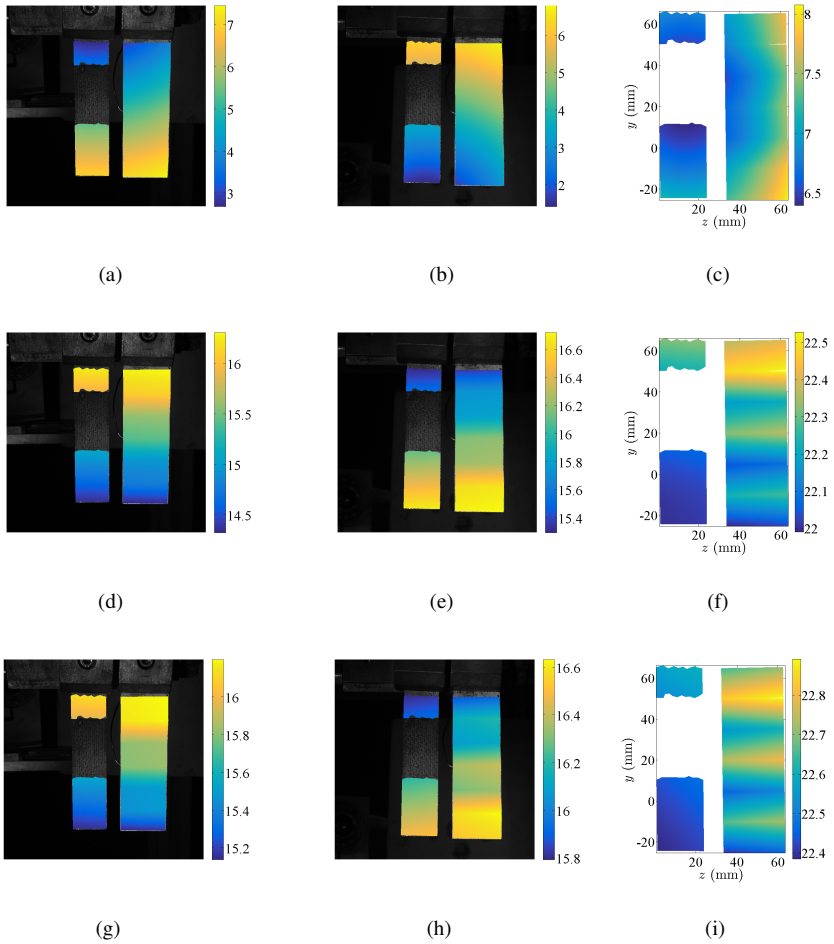

Fig. 8 Sensitivity fields expressed in mpx/µm of the stereovision system. Each row reports the results for X, Y and Z-directions. The first column corresponds to camera #1, the second to camera #2, and the third to the total sensitivity projected onto the nominal shape of the plate and the calibration target.

planar as opposed to the calibration target that has a roof top like shape (Figure 18), which increases the RMS levels.

4 Uncertainty Quantifications

4.1 Experimental Protocol

The following analyses only correspond to the very first part of the experiment [39], namely, images were acquired at room temperature for different positions of the calibration target and the sample [19] for UQ purposes. It will be referred to as UQ phase. The sequence of prescribed in-plane displacements was conducted thanks to the in-plane $Y-Z$ micro positioning stage available on the setup. For each of the 23 positions (Table 2) approximately 15 image pairs were recorded. This procedure was repeated when the fan was turned on to quantify its effect on heat waves mitigation at room temperature, as commonly used in reported high-temperature experiments [41,42,43,44,45], and on spurious vibrations that may occur.

Table 2 $Y-Z$ in-plane prescribed displacements with the micro-positioning linear stage for the UQ phase.

Step	Y disp. (mm)	Z disp. (mm)
1	0	0
2	-10^{-3}	0
3	-2×10^{-3}	0
4	-5×10^{-3}	0
5	-0.01	0
6	-0.05	0
7	-0.1	0
8	-0.5	0
9	-1	0
10	-2	0
11	-4	0
12	0	0
13	0	10^{-3}
14	0	2×10^{-3}
15	0	5×10^{-3}
16	0	0.01
17	0	0.05
18	0	0.1
19	0	0.5
20	0	1
21	0	2
22	0	4
23	0	0

4.2 A Priori Estimates

Equations (8) and (11) enable the standard displacement uncertainties to be estimated once the placement sensitivities (Figure 8), the mean RMS image gradient, and acquisition noise levels are known. For the latter, 2D-DIC analyses were run on each image series of the first UQ step. This is possible since the master meshes (Figures 19 and 25) were projected onto the reference images acquired by both cameras thanks to the calibrated projection matrices $[\boldsymbol{P}^c]$ (see Figure 9). For the CMC surface, the master mesh has a mean size (*i.e.,* square root of the mean surface of the T3 elements) of 1.5 mm. The mesh of the calibration target has a mean size of 1.7 mm. When reprojected onto the reference pictures, the corresponding mesh sizes are 25 px and 26 px, respectively.

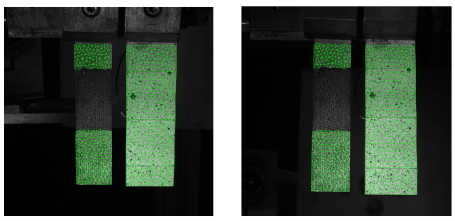

(a) (b)

Fig. 9 Projected meshes onto the reference pictures acquired by cameras #1 (a) and #2 (b).

At the end of these 2D analyses, the gray level residuals were stored. For each pixel, the standard deviation of the residuals was computed, and the mean over the ROI was evaluated. A 2/3 correction was finally applied since a bilinear gray level interpolation scheme was considered [27]. For the calibration target and the CMC surface, $\sqrt{2}\sigma^1 = \sqrt{2}\sigma^2 = 1.3$ gray level. It is worth noting the $\sqrt{2}$ factor is related to the fact that gray level residuals correspond to gray level differences of two images (*i.e.,* its variance is twice that of acquisition noise).

With all these data at hand, it is possible to estimate a priori the standard displacement uncertainties by applying Equations (8) or (11). One additional information should be added, namely, if the number of integration points increases, pixels may be shared by more than one integration point [46]. In that case, no gain is expected in terms of measurement uncertainty since no additional information is available (*i.e.,* the standard displacement uncertainties no longer decrease). It follows that the equivalent number of integration points is defined by

$$N_{eq} = \min(N_{IP}, N_{px}) \tag{27}$$

where N_{px}^2 denotes the number of pixels contained, on average, in each element of the projected meshes. In the present case, the maximum value is equal to 26^2 (see Table 3), and thus $N_{px} = 26$.

Figure 10 shows the corresponding estimates for the CMC surface and the calibration target. Because of the previous modification of the equivalent number of integration points, a flattening of the different curves is observed. When using Equation (8), the predictions are stopped when $N_{IP} = N_{px}$. The same dependence with the number of integration points is observed for both approaches. As expected from the sensitivity fields, the uncertainty level for the out-of-plane displacements is about three times higher than for in-plane displacements. Overall, the expected uncertainty levels are similar for the CMC surface and and the calibration target.

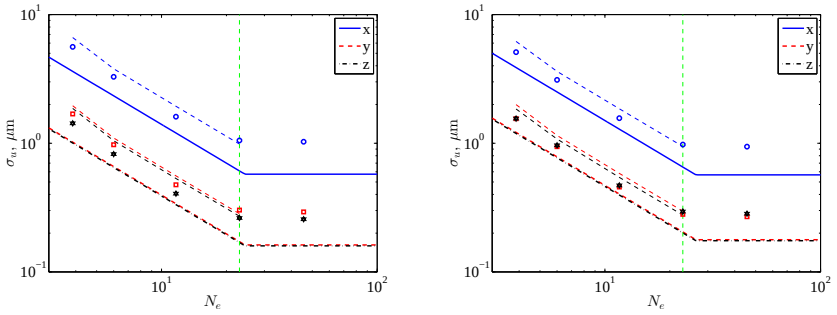

Fig. 10 A priori estimates of the standard displacement uncertainties as functions of the equivalent number of integration points according to Equations (11) and (27) (thick lines) and Equation (8) (thin dashed lines) compared to actual results for the artificial test case (symbols) for the CMC surface (a) and calibration target (b). The vertical (green) dashed line depict the number of integration points that was selected for the analysis of the UQ phase.

These estimates are compared to an artificial case that consisted in considering the images of the reference configuration, and adding white Gaussian noise with variances consistent with actual acquisition noise of both cameras. The same number of images was considered as that of step 1 of the UQ phase. Stereocorrelation analyses were run on this set of artificial pictures for different numbers of integration points. From these results, the standard displacement uncertainties for any component were obtained as the square root of the average nodal variances and are reported in Figure 10 as symbols. For both surfaces, a very good agreement is observed with the a priori estimates following Equations (8) and (27). Conversely, the approximate solution given by Equation (11) (with a 1.16 prefactor) combined with Equation (27) provides lower bound estimates. This result shows that if uncertainty levels are sought with high fidelity, the full covariance matrix should be computed.

From this artificial test case, it is concluded that Equations (11) and (27) are validated for the CMC surface and calibration target. Such results also allow the user to select the optimal number of integration points associated with the selected discretization. In the present case, $N_{IP}^2 = 528$ is the best choice since it allows the measurement uncertainty to be lowered as much as possible (see green dashed lines in Figure 10). It was kept for the following analyses of the whole UQ phase (Table 3).

4.3 Analyses of the UQ phase

The 707 image pairs acquired during the UQ phase (without or with fan) were analyzed. Table 3 gathers all stereocorrelation analysis parameters of the UQ phase.

Table 3 Stereocorrelation analysis parameters

DIC software	Correli 3.0 [47]
Image filtering	None
Element sizes	1.5-1.7 mm ($\approx 25-26$ px, see Figure 9)
Shape functions	Linear (T3 elements)
Evaluation points (per element)	528 (*i.e.,* $N_{IP} \approx 23$)
Matching criterion	Normalized quadratic differences (1)
Interpolant	Linear
Displacement noise-floor	see text and Figures 13, 15

3D surface displacement fields were measured on the calibration target, the standard displacement uncertainties were computed for each prescribed position. For each position of the calibration target prescribed by the in-plane linear stage (Table 2), approximately 15 images were acquired. Thus, it was possible to investigate the uncertainty on the displacements measured by stereocorrelation on each set of 15 images. Figure 11 shows the uncertainty maps computed for each component of displacements (namely the out-of-plane

U_x, the longitudinal U_y and the transverse U_z displacements) for, respectively, the initial position of the calibration target and for a prescribed displacement of $U_y^{presc.}$ = 2 mm, when the fan was off.

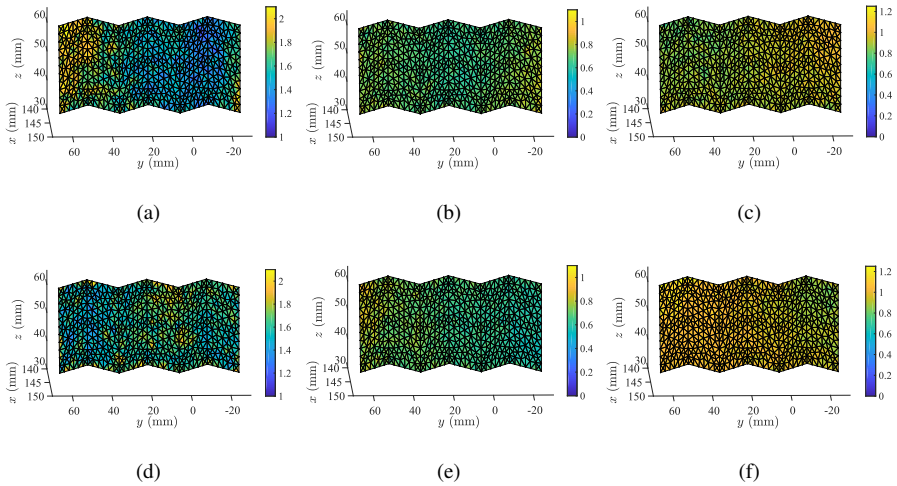

Fig. 11 Standard uncertainty maps for (a,d) out-of-plane U_x, (b,e) longitudinal U_y and (c,f) transverse U_z displacement fields (expressed in µm) of the calibration target computed for the first calibration step (initial position) with no fan (top row) and the tenth calibration step ($U_y^{presc.}$ = 2 mm) with no fan (bottom row).

The uncertainty maps are rather homogeneous, which was expected since the entire surface of the calibration target was speckled and for a given position, the lighting conditions did not vary much with time. It can be noted that the uncertainty levels were of the same order for both prescribed conditions. This observation is also evidenced when plotting the average of the nodal uncertainties for each increment of the calibration phase (Figure 12).

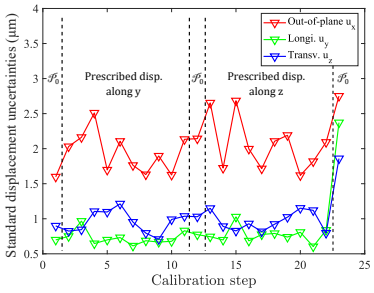

Fig. 12 Change of standard displacement uncertainties during the UQ phase for out-of-plane U_x (in red), longitudinal U_y (in green) and transverse U_z (in blue) displacements of the calibration target. The vertical dashed lines mark the ends of the main steps of the UQ phase, namely the acquisition at initial position $\mathscr{P}_0$, for displacements along Y-direction and for Z-direction.

The standard displacement uncertainties were virtually constant for *any* position, except the very last increment. During that step, the measured displacements were consistent with the prescribed position (*i.e.,* return to the initial position, implying null-displacements), except for one image of the series where displacements of ≈ 5 µm were measured for the Y and Z-directions. This spurious motion induced higher standard deviations for the corresponding increment, so that it was excluded from the following uncertainty analyses. The longitudinal displacement U_y was characterized by the lowest level of uncertainty (*i.e.,* 0.7 µm). The uncertainty of the transverse displacement U_z was higher, with a mean level over the different positions of the UQ phase of 1 µm. Regarding the out-of-plane displacement U_x, the uncertainty level was 2.7 times higher than that of the longitudinal component and was equal to 2 µm.

Moreover, since the UQ phase was repeated while the fan was on, it was possible to analyze in the same way the displacement uncertainties (Figure 13). There are no significant differences between the two configurations (*i.e.,* with and with no fan) because there were

no detectable heat waves at room temperature in this experiment and the air flow was smooth enough (laminar) not to induce detectable vibrations. The source of heat for the surrounding air, which could be due to the lighting devices, was several tens of centimeters away from the observed surfaces. The a priori estimates based upon Equation (8) led to the following levels: 1 µm for U_x, 0.3 µm for both in-plane directions (Figure 10(b)). The mean ratio of a posteriori results to a priori estimates is only 2.1. Given the fact that other sources of uncertainties are involved, this level is considered rather low.

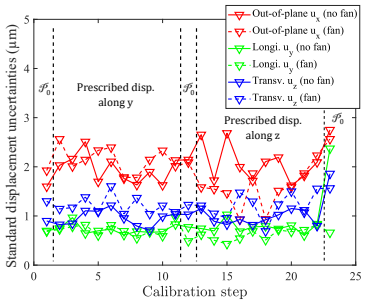

Fig. 13 Change of standard displacement uncertainties during the UQ phase for out-of-plane U_x (in red), longitudinal U_y (in green) and transverse U_z (in blue) displacements of the calibration target. The results are reported when the fan was off (solid lines) and on (dashed lines). The vertical dashed lines mark the ends of the main steps of the UQ phase, namely, the acquisitions at initial position $\mathscr{P}_0$, for displacements along Y-and Z-directions.

Similar results were obtained using the displacements measurements on the CMC surface during the UQ phase with the same level of uncertainties on the three components. Figure 14 illustrates the uncertainty maps related to the CMC sample.

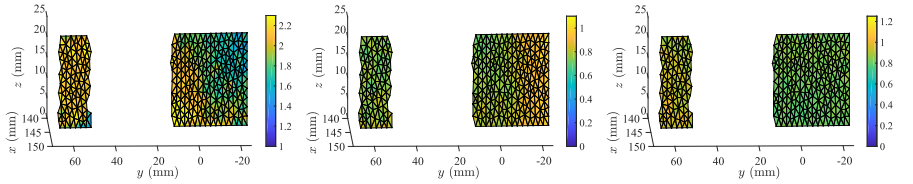

Fig. 14 Standard uncertainty maps for (a) out-of-plane U_x, (b) longitudinal U_y and (c) transverse U_z displacements (expressed in µm) of the CMC sample computed for the first UQ step (initial position) with no fan.

Figure 15 shows the history of standard uncertainties on CMC surface displacements for the UQ phase. The same comment can be made on the uncertainties computed for the last increment, since the global motions measured on one image affected both the calibration target and the CMC sample, leading to increased standard deviations for that increment. Regarding the other positions, the uncertainty levels were stable, with average values over the 22 calibration increments of 2 µm for the out-of-plane component U_x, 0.8 µm for the longitudinal displacement U_y and 0.9 µm for the transverse displacement U_z. Last, it is worth noting that the fluctuations of the uncertainties reported in Figures 13 and 15 are totally correlated. This trend is to be expected since the calibration target *and* the CMC surface were imaged at the same time (Figure 9).

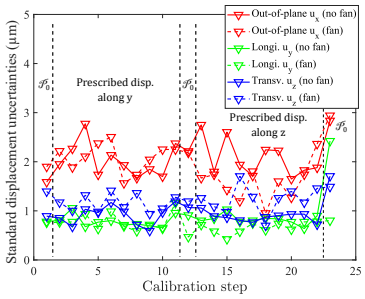

Fig. 15 Change of CMC standard displacement uncertainties during the calibration phase for out-of-plane u_x (in red), longitudinal u_y (in green) and transverse u_z (in blue) displacements of the CMC sample. The results are reported when the fan is off (solid lines) and on (dashed lines). The vertical dashed lines mark the ends of the main steps of the calibration phase, namely the acquisitions at initial position $\mathscr{P}_0$, for displacements along Y-direction and for Z-direction.

The a priori estimates based upon Equation (8) were equal to 1 µm for U_x, and 0.3 µm for both in-plane directions (Figure 10(a)). The mean ratio of the a posteriori results to a priori estimates is equal to 2.1, which again remains very low.

Since the UQ phase was performed a few hours before the heating phases of the experiment [39], a similar analysis based on the first 46 images acquired at room temperature just at the beginning of the actual test, was conducted to confirm the previous estimates. The uncertainty maps shown in Figure 16 were measured on the calibration target.

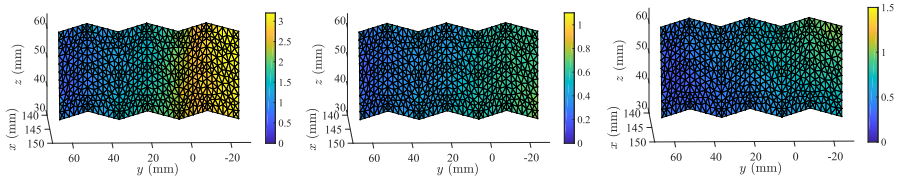

(a) (b) (c)

Fig. 16 Uncertainty maps associated with (a) out-of-plane U_x, (b) longitudinal U_y and (c) transverse U_z displacements (expressed in µm) measured on the calibration target at room temperature (before heating), with no fan

The standard deviations were lower than in the previous analyses, namely, equal to 1.8 µm for the out-of-plane component and 0.5 µm for the in-plane displacements. The low-range heterogeneity on the uncertainty maps may be due to differences in lighting conditions. When compared to the a priori estimates, the ratio is equal to 1.8.

5 Conclusion

Displacement uncertainties were assessed in the case of T3-stereocorrelation. Mean field approximations were performed to derive a priori estimates for different meshes made of T3 elements. Closed-form solutions were obtained for the Hessian and covariance matrices in the case of simple meshes. When more than one element is used, there are significant gains to be expected for the nodal displacement uncertainties (*e.g.,* a factor 6 on the variances of inner nodes). Further, very simple lower bounds were obtained. In its simplest declination, the standard displacement uncertainty depends upon the image contrast (characterized by its RMS level), the mean placement sensitivities (which depend on the extrinsic and intrinsic parameters of each camera), acquisition noise (*i.e.,* camera hardware and illumination), and the number of integration points.

Such framework allows a priori estimates of displacement uncertainties to be obtained. They were probed at room temperature when applied to an experimental setup in which thermomechanical tests are to be performed by illuminating the top surface of ceramic matrix composites with a laser beam. An in-situ calibration target was designed to ensure a good calibration of a stereovision system using a *single* pair of images and measure small displacements, as expected for SiC/SiC composites. This configuration allows, in particular, heat haze effects to be analyzed in-situ [39].

Uncertainty quantifications were performed by acquiring sets of pictures for different positions of the calibration target *and* the sample [19]. Both surfaces were studied and the corresponding measurement uncertainties were assessed. No degradation was observed for the range of prescribed displacements. A fan was also turned on to investigate its effect for room temperature evaluations. No major effect was observed. The displacement uncertainties showed the high-quality of the stereovision setup and its calibration, with levels less than 1 µm for the in-plane measurements and about 2 µm for the out-of-plane component. When compared to a priori estimates, there was only a factor 2 difference with respect to the lower bounds derived herein. This observation shows that there are other sources of random or systemic uncertainties, yet they remain reasonably small.

Since the calibration target can be kept in high temperature tests, the impact of high-temperature environments on the measurement trustworthiness of 3D surface displacements and the level of displacement fluctuations can be compared with respect to the present uncertainty levels obtained at room temperature. A future study will focus on such effects at high temperatures.

Acknowledgements This work was supported within PRC MECACOMP, a French research project co-funded by DGAC and SAFRAN Group, managed by SAFRAN Group and involving SAFRAN Group, ONERA and CNRS.

6 Compliance with Ethical Standards

The authors have no conflict of interest to declare.

References

1. M.A. Sutton, J.J. Orteu, and H. Schreier. *Image correlation for shape, motion and deformation measurements: Basic Concepts, Theory and Applications*. Springer, New York, NY (USA), 2009.
2. J.J. Orteu. 3-D computer vision in experimental mechanics. *Optics and Lasers in Engineering*, 47:282–291, 2009.
3. M.A. Sutton. Computer vision-based, noncontacting deformation measurements in mechanics: A generational transformation. *Applied Mechanics Reviews*, 65(AMR-13-1009):050802, 2013.
4. P.F. Luo, Y.J. Chao, M.A. Sutton, and W.H. Peters. Accurate measurement of three-dimensional deformations in deformable and rigid bodies using computer vision. *Experimental Mechanics*, 33:123–132, 1993.
5. P.F. Luo, Y.J. Chao, and M.A. Sutton. Application of stereo vision to three-dimensional deformation analyses in fracture experiments. *Optical Engineering*, 33(3):981–990, 1994.
6. J.D. Helm, S.R. McNeill, and M.A. Sutton. Improved three-dimensional image correlation for surface displacement measurement. *Optical Engineering*, 35(7):1911–1920, 1996.
7. J.-J. Orteu, V. Garric, and M. Devy. Camera calibration for 3D reconstruction: application to the measurement of 3D deformations on sheet metal parts. In Philippe Refregier and Rolf-Juergen Ahlers, editors, *New Image Processing Techniques and Applications: Algorithms, Methods, and Components II*, volume 3101, pages 252–263. International Society for Optics and Photonics, SPIE, 1997.
8. P.J. Besl and N.D McKay. Method for registration of 3-d shapes. In *Sensor Fusion IV: Control Paradigms and Data Structures*, volume 1611, pages 586–607. International Society for Optics and Photonics, 1992.
9. L. Zhu, J. Barhak, V. Srivatsan, and R. Katz. Efficient registration for precision inspection of free-form surfaces. *The International Journal of Advanced Manufacturing Technology*, 32(5-6):505–515, 2007.

10. N. Senin, B.M. Colosimo, and M. Pacella. Point set augmentation through fitting for enhanced icp registration of point clouds in multisensor coordinate metrology. *Robotics and Computer-Integrated Manufacturing*, 29(1):39–52, 2013.

11. F. Hild and S. Roux. Method of three-dimensional stereo-correlation measurements using a parametric representation of the measurement object. Patent family FR2991448B1, EP2856424B1, US9733071B2, ES2700975T3, 2012.

12. B. Beaubier, J.E. Dufour, F. Hild, S. Roux, S. Lavernhe-Taillard, and K. Lavernhe-Taillard. CAD-based calibration of a 3D-DIC system: Principle and application on test and industrial parts. *Experimental Mechanics*, 54(3):329–341, 2014.

13. L. Dubreuil, J.-E. Dufour, Y. Quinsat, and François Hild. Mesh-based shape measurements with stereo-correlation. *Experimental Mechanics*, 56(7):1231–1242, 2016.

14. D. Etievant, Y. Quinsat, F. Thiebaut, and F. Hild. A modal approach for shape defect measurement based on global stereocorrelation. *Optics and Lasers in Engineering*, 128:106030, 2020.

15. J.-E. Dufour, B. Beaubier, F. Hild, and S. Roux. CAD-based displacement measurements. Principle and first validations. *Experimental Mechanics*, 55(9):1657–1668, 2015.

16. J.-E. Dufour, F. Hild, and S. Roux. Shape, Displacement and Mechanical Properties from Isogeometric Multiview Stereocorrelation. *Journal of Strain Analysis for Engineering Design*, 50(7):470–487, 2015.

17. J.E. Dufour, B. Beaubier, S. Roux, and F. Hild. Displacement measurement using CAD-based stereo-correlation with meshes. In *ICEM conference*, 2014.

18. J.-E. Pierré, J.-C. Passieux, and J.-N. Périé. Finite Element Stereo Digital Image Correlation: Framework and Mechanical Regularization. *Experimental Mechanics*, 57(3):443–456, 2017.

19. ASD-STAN prEN 4861 P1. Metrological assessment procedure for kinematic fields measured by digital image correlation, 2018.

20. E.M.C. Jones and M.A. Iadicola (Edts.). *A Good Practices Guide for Digital Image Correlation*. International Digital Image Correlation Society (iDICs), idics.org/guide/, DOI: 10.32720/idics/gpg.ed1, 2018.

21. Y.-Q. Wang, M. A. Sutton, X.-D. Ke, H. W. Schreier, P. L. Reu, and T. J. Miller. On Error Assessment in Stereo-based Deformation Measurements. *Experimental Mechanics*, 51(4):405–422, 2011.

22. X.-D. Ke, H. W. Schreier, M. A. Sutton, and Y. Q. Wang. Error Assessment in Stereo-based Deformation Measurements. *Experimental Mechanics*, 51(4):423–441, 2011.

23. P.L. Reu. A study of the influence of calibration uncertainty on the global uncertainty for digital image correlation using a monte carlo approach. *Experimental Mechanics*, 53(9):1661–1680, 2013.

24. C. Zhu, S. Yu, C. Liu, P. Jiang, X. Shao, and X. He. Error estimation of 3D reconstruction in 3D digital image correlation. *Measurement Science and Technology*, 30(2):025204, 2019.

25. R. Balcaen, L. Wittevrongel, P. L. Reu, P. Lava, and D. Debruyne. Stereo-DIC Calibration and Speckle Image Generator Based on FE Formulations. *Experimental Mechanics*, 57(5):703–718, 2017.

26. R. Balcaen, P.L. Reu, P. Lava, and D. Debruyne. Stereo-dic uncertainty quantification based on simulated images. *Experimental Mechanics*, 57(6):939–951, 2017.

27. F. Hild and S. Roux. Displacement uncertainties with multiview correlation schemes. *Journal of Strain Analysis for Engineering Design*, 55(7-8):199–211, 2020.

28. C.R. Rao. Information and the accuracy attainable in the estimation of statistical parameters. *Bulletin of the Calcutta Mathematical Society*, 37:81–89, 1945.

29. H. Cramér. *Mathematical Methods of Statistics*. Princeton Univ. Press, Princeton, NJ (USA), 1946.

30. T. Archer. *Comportement sous gradients thermiques d'un composite à matrice céramique revêtu*. PhD thesis (in French), Université Paris-Saclay, 2019.

31. F.J. Anscombe. The transformation of Poisson, binomial and negative-binomial data. *Biometrika*, 35(3/4):246–254, 1948.

32. F. Sur and M. Grediac. Sensor noise modeling by stacking pseudo-periodic grid images affected by vibrations. *IEEE Signal Processing Letters*, 21(4):432–436, 2014.

33. J. Curt, M. Capaldo, F. Hild, and S. Roux. Optimal digital color image correlation. *Optics and Lasers in Engineering*, 127:105896, 2020.

34. B.D. Lucas and T. Kanade. An iterative image registration technique with an application to stereo vision. In *7th International Joint Conference on Artificial Intelligence*, pages 674–679, 1981.

35. F. Hild and S. Roux. Digital image correlation. In P. Rastogi and E. Hack, editors, *Optical Methods for Solid Mechanics. A Full-Field Approach*, pages 183–228, Weinheim (Germany), 2012. Wiley-VCH.

36. F. Hild and S. Roux. Comparison of local and global approaches to digital image correlation. *Experimental Mechanics*, 52(9):1503–1519, 2012.

37. E. Bouillon, B. Lacombe, and Y. Richard. 10th International Conference on High Temperature Ceramic Matrix Composites (HT-CMC 10). page 371, 2019.

38. D. Demange, P. Beauchêne, M. Bejet, and R. Casulleras. Mesure simultanée de la diffusivité thermique selon les deux directions principales d'un matériau. *Revue Générale de Thermique*, 36(10):755–770, 1997.

39. M. Berny. *High-temperature tests for ceramic matrix composites: from full-field regularised measurements to thermomechanical parameter identification*. PhD thesis, Paris-Saclay University, 2020.

40. M. Vitse, M. Poncelet, A.E. Iskef, J.-E. Dufour, R. Gras, A. Bouterf, B. Raka, C. Giry, F. Gatuingt, F. Hild, F. Ragueneau, and S. Roux. Toward virtual design and optimization of a structural test monitored by a multi-view system. *Journal of Strain Analysis for Engineering Design*, DOI: 10.1177/0309324720910887, 2021.

41. J.S. Lyons, J. Liu, and M.A. Sutton. High-temperature deformation measurements using digital-image correlation. *Experimental Mechanics*, 36(1):64–70, 1996.

42. M.D. Novak and F.W. Zok. High-temperature materials testing with full-field strain measurement: Experimental design and practice. *Review of Sicentific Instruments*, 82(11):115101, 2011.

43. J.T. Hammer, J.D. Seidt, and A. Gilat. Strain measurement at temperatures up to 800 °c utilizing digital image correlation. In H. Jin, C. Sciammarella, S. Yoshida, and L. Lamberti, editors, *Advancement of Optical Methods in Experimental Mechanics, Volume 3: Conference Proceedings of the Society for Experimental Mechanics Series*, pages 167–170. Springer International Publishing, 2014.

44. P. Leplay, O. Lafforgue, and F. Hild. Analysis of Asymmetrical Creep of a Ceramic at 1350°C by Digital Image Correlation. *Journal of the American Ceramic Society*, 98(7):2240–2247, 2015.

45. E.M.C. Jones and P.L. Reu. Distortion of Digital Image Correlation (DIC) Displacements and Strains from Heat Waves. *Exp. Mech.*, 58:1133–1156, 2018.

46. C. Minguet, F. Soulas, T. Lafargue-Tallet, E. Chalumeau, M. Pommies, R. Peiffer, and F. Hild. On the Validation of A Priori Estimates of Standard Displacement Uncertainties in T3-Stereocorrelation. *Measurement Science and Technology*, 32(2):024004, 2021.

47. H. Leclerc, J. Neggers, F. Mathieu, F. Hild, and S. Roux. *Correli 3.0*. IDDN.FR.001.520008.000.S.P.2015.000.31500, Agence pour la Protection des Programmes, Paris (France), 2015.

48. Y. Morvan. *Acquisition, compression and rendering of depth and texture for multi-view video*. PhD thesis, Eindhoven University of Technology, 2009.

Appendix A: Calibration Target

To calibrate the stereovision system, a new calibration target (Figure 17) was designed. One face of the calibration target is composed of a series of six inclined planes with a vertical offset of 3 mm, corresponding to the cameras depth of field. The shape of the opposite face is identical, with an offset of 1 mm. The object was speckled with black paint RAL 9005 by Ront®. The calibration target that includes 14 corners (*i.e.,* fiducials) at different heights within the field of view of the cameras allows for a good initialization of the projection matrices $[\boldsymbol{P}^1]$ and $[\boldsymbol{P}^2]$, and the calibration of the stereovision system with a *single* pair of images (contrary to what is usually carried out with planar calibration targets [1] that require full sets of different positions). Moreover, this shape enables for the calibration within a volume corresponding to the expected deformation of CMC samples. Last, in the present configuration, the calibration target was kept in the field of view during whole experiments [39].

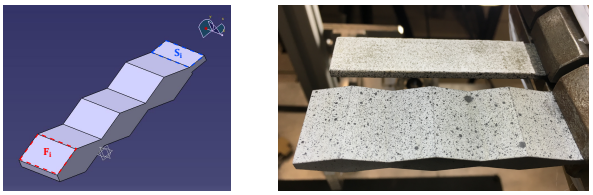

(a) (b)

Fig. 17 (a) CAD model of the calibration target where a facet is denoted F_i and an edge surface S_i. (b) Speckled calibration target positioned next to a tested CMC sample.

To perform the first calibration step, the real model of the manufactured calibration target was identified. First, a 3D surface measurement was performed using a Coordinate-Measuring Machine. For each main facet of the object (inclined planes, denoted as F_i in

Figure 17(a)), the space coordinates of 50 points, uniformly distributed over the surface, were acquired. For each of the two small surfaces (horizontal planes S_i), 10 points were acquired.

A total of 620 points was used to build the model of the calibration target. Then, an algorithm based on least squares and least distances methods was implemented to find the best surface interpolating all the points of a facet [39]. It is a two-step algorithm, where the first step was based on least squares fit between the measurements and the estimated plane, and the second step on the least distances method to update the plane normal direction. With such procedure, a more faithful parameterization of the surface is achieved in comparison to the nominal shape, *and* minimizes the distance of the measured points to the sought plane. Once the optimization of each face model was performed, all planes were combined to determine the corners of every facet. Then, the global model for the calibration target was constructed and can be expressed in different frameworks, either using an FE (T3) mesh or NURBS patches (Figure 18).

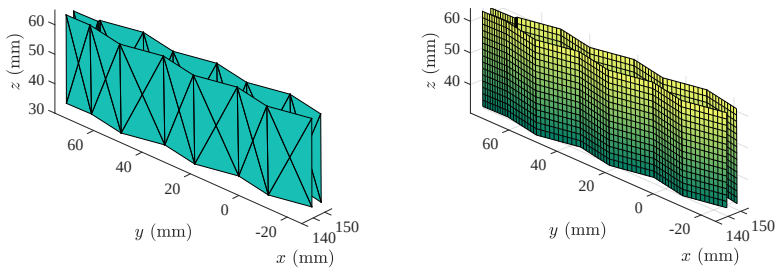

(a) (b)

Fig. 18 (a) Finite Element model and (b) corresponding NURBS model of the calibration target.

Appendix B: Calibration of the Two Cameras

The calibration procedure aims to minimize the cost function [12]

$$\phi_c^2([\boldsymbol{P}^1],[\boldsymbol{P}^2]) = \sum_{j=1}^{n_s} \sum_{\boldsymbol{X}_j \in \mathscr{S}_j} \left(\frac{I_0^1(\boldsymbol{x}^1(\boldsymbol{X}_j,[\boldsymbol{P}^1]))}{2(\sigma^1)^2} - \frac{I_0^2(\boldsymbol{x}^2(\boldsymbol{X}_j,[\boldsymbol{P}^2]))}{2(\sigma^2)^2} \right)^2 \tag{28}$$

with respect to the components of the projection matrices $[\boldsymbol{P}^1]$ and $[\boldsymbol{P}^2]$, where $\mathscr{S}_j$ denotes the $n_s = 6$ surfaces defining one side of the calibration target. The calibration procedure used herein was based an the FE formulation of global stereocorrelation [13]. A fine mesh of the calibration target was considered. It was composed of 558 T3 elements 1.7 mm in size (Figure 19). The total number of integration points was equal to 528 (*i.e.,* $N_{eq} \approx 23$) so that the projected surface of one integration point had the size of roughly one pixel in the images (Table 3).

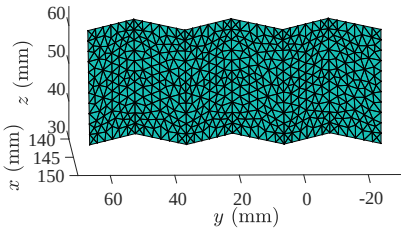

(a)

Fig. 19 Three-noded triangular (T3) mesh of the calibration target used for calibration procedure.

The minimization procedure was initialized with a direct estimation (via SVD [48,12]) of the projection matrices, using the 3D positions of the 14 fiducials (*i.e.,* corners of the calibration target) and their associated projection in each image, see Figure 20.

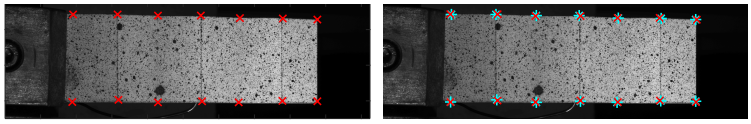

(a) (b)

Fig. 20 (a) Fiducials (in red crosses) on one of the image pair on the calibration target and (b) estimated 2D positions (in cyan asterisks) of these points through initial projection matrix obtained with an SVD pre-calibration, along with manually clicked points (in red crosses).

The associated gray level (GL) residuals using this initialization of the projection matrices are shown in Figure 21(a) for each camera. The initialization led to a medium level of RMS residuals (≈ 21.4 gray levels, *i.e.,* 8.4% of the dynamic range) and to errors on the description of the calibration target edges. This was expected since the initialization was obtained by using only 14 fiducials, which were manually selected on the images.

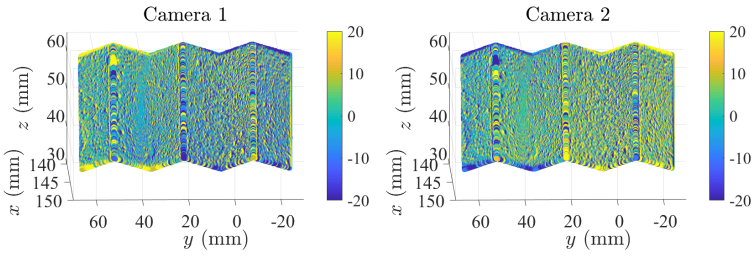

(a)

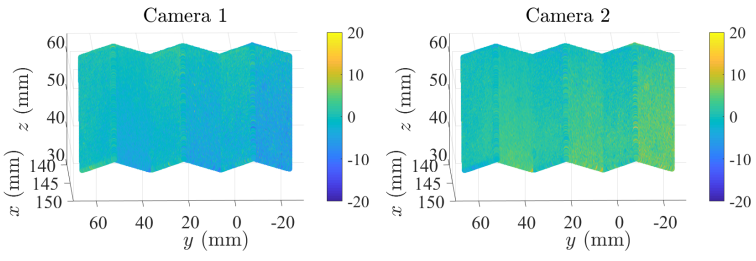

(b)

Fig. 21 Initial (a) and converged (b) gray level residual fields for each camera that was calibrated.

At the end of the optimization procedure, the calibration converged to a solution that considerably reduced the residuals (Figure 21(b)) to an RMS level of 3.1 gray levels (*i.e.,* 1.2% of the dynamic range). As opposed to Figure 21(a), the edges were well-defined and the errors on the speckled parts were erased, hence leading to a good stereosystem calibration. Figure 22 illustrates how each node was correctly projected onto each image plane and matched the calibration target shapes on the images (especially for the edges, the corners and the inclined planes).

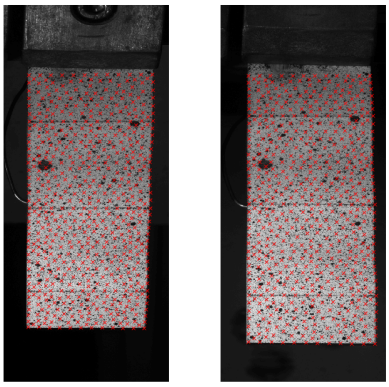

(a) (b)

Fig. 22 Projection of nodes of the calibration target mesh (depicted with red crosses) using the converged projection matrices for (a) camera #1 and (b) camera #2.

Appendix C: Shape Correction for the CMC Sample

Displacements were then measured for the top surface of the CMC sample. The first step consisted in expressing its model in the calibration target frame. The correction procedure seeks to determine the (new) nodal positions gathered in the column vector $\{\boldsymbol{N}\}$ of the

surface mesh by globally minimizing the cost function [13]

$$\phi_s^2(\{\boldsymbol{N}\}) = \sum_{j=1}^{n_s} \sum_{\boldsymbol{X}_j \in \mathscr{S}_j} \left(\frac{I_0^1(\boldsymbol{x}^1(\boldsymbol{X}_j, \{\boldsymbol{N}\}))}{2(\sigma^1)^2} - \frac{I_0^2(\boldsymbol{x}^2(\boldsymbol{X}_j, \{\boldsymbol{N}\}))}{2(\sigma^2)^2} \right)^2 \tag{29}$$

Since the goal was to correct the global position of the CMC surface with respect to the calibration target, the FE mesh was very simple (*i.e.,* made of two T3 elements covering the CMC surface). Because the discretization was coarse, a large number of integration points (*i.e.,* 8,256 corresponding to $N_{eq} \approx 91$) was selected. The nodal positions were initialized using in-situ distances between the sample and the calibration target. This initial model led to an RMS residual of 12.1 gray levels, corresponding to 4.7% of the dynamic range. The maps show that the residuals were higher on the right part (free edge) of the sample with a line of evaluation points with very high residuals (Figure 23(a)). They indicated that the real model of the CMC sample was shorter and needed to be corrected.

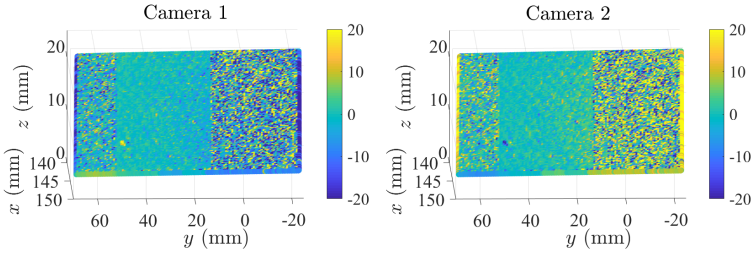

(a)

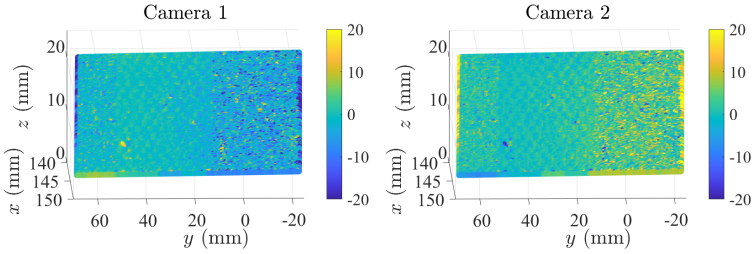

(b)

Fig. 23 Initial (a) and converged (b) gray level residuals for each camera and for the CMC sample using its optimized shape.

At convergence of the approach, the RMS residuals were reduced to 2.1% of the dynamic range (*i.e.,* 5.3 gray levels) and the previous errors at the free edge were virtually erased (Figure 23(b)). It was even possible to see the residuals associated with CMC 3D woven architecture of the central unspeckled part of the sample, which was a further proof of the good quality of the shape corrections.

The corrected position of the sample is shown in Figure 24. The main contribution is on the out-of-plane component U_x with a mean translation due to a wrong estimation of the sample thickness. There is also a gradient of $\approx$ 180 µm between the X-position of nodes in the clamp (corresponding to $Y \approx 60$ mm) and the nodes of the free edge, explained by the fact that the CMC sample was slightly inclined at the free edge. Regarding the components

on the longitudinal Y and transverse Z-directions, the corrections mainly corresponded to an adjustment of the shape in terms of length and width.

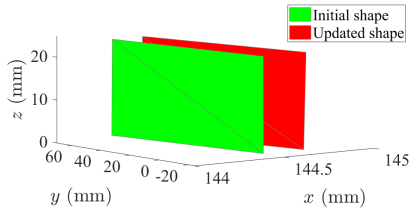

Fig. 24 Comparison between the initial (green mesh) and optimized (red mesh) positions of the CMC surface.

Once the position of the sample was corrected, it was possible to measure its 3D surface displacements. A fine mesh was used with 498 T3 elements of mean size 1.5 mm (Table 3). To avoid convergence issues on displacement measurements, this mesh did not contain the unspeckled part and a line of nodes at the clamped edge, since they were hidden on one camera plane. Figure 25 shows the mesh with its projection onto both camera planes.

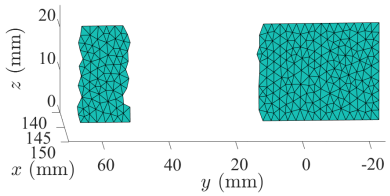

(a)

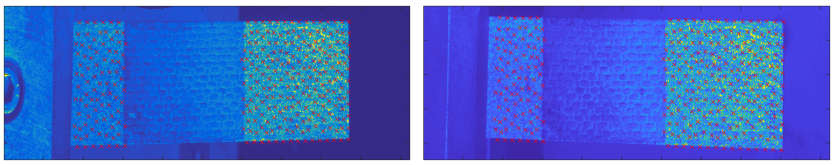

(b) (c)

Fig. 25 (a) Mesh of the CMC surface and projection of its nodes (red crosses) using the converged shape corrections for (b) camera #1 and (c) camera #2.

With this last step, the cameras were calibrated *and* the reference configuration of the CMC surface was expressed in the same frame. Displacement fields of the CMC surface *and* the calibration target can now be measured and are reported in a *unique* frame.